

Cite this: *J. Mater. Chem. A*, 2020, **8**, 3344

# Core–shell nanoporous AuCu<sub>3</sub>@Au monolithic electrode for efficient electrochemical CO<sub>2</sub> reduction†

Xiaoming Ma,<sup>‡a</sup> Yongli Shen,<sup>‡a</sup> Shuang Yao,<sup>a</sup> Cuihua An,<sup>ID a</sup> Weiqing Zhang,<sup>ID \*a</sup> Junfa Zhu,<sup>ID c</sup> Rui Si,<sup>ID \*b</sup> Chunxian Guo<sup>ID d</sup> and Changhua An<sup>ID \*a</sup>

Selective conversion of carbon dioxide (CO<sub>2</sub>) to a reusable form of carbon *via* electrochemical reduction has attracted intensive interest for the storage of renewable energy. However, the achievement of efficient bulk monolithic electrocatalysts still remains a challenge. Herein, a facile oxidative etching of the Au<sub>20</sub>Cu<sub>80</sub> alloy was developed for the synthesis of a monolithic nanoporous core–shell structured AuCu<sub>3</sub>@Au electrode, which showed a faradaic efficiency (FE) of 97.27% with a partial current density of 5.3 mA cm<sup>-2</sup> at -0.6 V vs. RHE for the production of CO. The FE value is about 1.45 times higher than that over the Au nanocatalyst. Unlike single nanoporous Au, AuCu<sub>3</sub>@Au maintained an excellent performance in a broad potential window. Furthermore, a 23 cm long nanoporous AuCu<sub>3</sub>@Au bulk electrode with good ductility was prepared, over which the active current reached up to 37.2 mA with a current density of 10.78 mA cm<sup>-2</sup> at -0.7 V vs. RHE, pushing the reduction of CO<sub>2</sub> to industrialization. The unsaturated coordination environment with a coordination number of 8.2 over the shell gold and curved interface determined this high electrocatalytic performance. Density functional theory calculations suggested that the double-dentate adsorption structure in the AuCu<sub>3</sub>@Au catalyst effectively improves the stability of the \*COOH intermediate. The density of states indicates that the introduction of Cu causes the d-band-centre of AuCu<sub>3</sub>@Au to move toward the Fermi level, directly bonding with \*COOH. Therefore, the adsorption of \*COOH on the surface of the AuCu<sub>3</sub>@Au catalyst is strengthened, facilitating the formation of CO. This work opens an avenue to achieve self-supported porous electrodes for various useful catalytic conversions.

Received 28th August 2019  
Accepted 6th January 2020

DOI: 10.1039/c9ta09471g

rsc.li/materials-a

## 1. Introduction

Electrochemical reduction of carbon dioxide (CO<sub>2</sub>) to value-added products in aqueous solution is a simple and promising strategy to decrease the concentration of CO<sub>2</sub> in the atmosphere and an appealing approach to store renewable energy.<sup>1–4</sup> Carbon monoxide (CO) is an attractive product due to

its broad applications as a gas precursor for industrial chemical manufacturing. Since Hori and coworkers found that Au foil has the capacity to reduce CO<sub>2</sub> to CO, it has been an essential element in important processes.<sup>5</sup> Additionally, its performance can be boosted by tuning its size,<sup>6–9</sup> shape,<sup>10–12</sup> and composition.<sup>13–15</sup> However, the high cost of Au prevents its widespread application. Thus, alloying Au to a non-precious metal without compromising its efficiency has been demonstrated as an effective strategy to design electrocatalysts. Furthermore, the control of the microstructure over nanoalloys provides an effective strategy to engineer high activity and selectivity in catalysts.<sup>16–18</sup> Especially, interface engineering with favourable core–shell nanostructures<sup>19–21</sup> is beneficial for enhancing the electrocatalytic performance of materials by adjusting their conductivity, charge transfer, and couple effects. For example, stable Au@Fe core–shell nanoparticles can be evolved from Au–Fe nanoalloy catalysts *via* the leaching of surface Fe, exhibiting superior CO selectivity, long term stability, and nearly a 100-fold increase in mass activity toward the CO<sub>2</sub> RR compared with single Au nanoparticles.<sup>22</sup>

In most cases, catalysts are fabricated *via* the deposition of synthesized nanoparticles on conductive supports; however, this

<sup>a</sup>Tianjin Key Laboratory of Organic Solar Cells and Photochemical Conversion, School of Chemistry and Chemical Engineering, Tianjin Key Laboratory of Advanced Functional Porous Materials, Institute for New Energy Materials & Low-Carbon Technologies, Tianjin University of Technology, Tianjin 300384, P. R. China. E-mail: zhangweiqing2008@hotmail.com; anch@tjut.edu.cn

<sup>b</sup>Shanghai Synchrotron Radiation Facility, Shanghai Institute of Applied Physics, Chinese Academy of Sciences, Shanghai, 201204, China. E-mail: sirui@sirui.sinap.ac.cn

<sup>c</sup>National Synchrotron Radiation Laboratory, University of Science and Technology of China, Hefei, Anhui 230029, People's Republic of China

<sup>d</sup>Institute for Advanced Materials and Devices, Suzhou University of Science and Technology, Suzhou 215009, China

† Electronic supplementary information (ESI) available. See DOI: 10.1039/c9ta09471g

‡ These two authors contributed equally to this work.

results in the degradation of the support and nanoparticle aggregation during long reactions.<sup>18</sup> Also, nanoporous metals possess intrinsic good conductivity and three-dimensional porous networks made of interconnected backbones (ligaments) and pores (channels/voids) on the nanoscale, enabling them to accelerate the electron transport.<sup>23</sup> These intrinsic merits render them as a class of promising electrocatalysts towards the CO<sub>2</sub> RR.<sup>24</sup> Recently, Jiao and co-workers fabricated a nanoporous Ag electrode with curved surfaces, which was capable of reducing CO<sub>2</sub> to CO with a 92% Faraday efficiency (FE) and a relatively high current density of 18 mA cm<sup>-2</sup> at -0.6 V (vs. RHE).<sup>25</sup> Zhang *et al.* found that porous Au has good activity for the reduction of CO<sub>2</sub> to CO, where low-coordinated gold atoms as active sites boosted its electrocatalytic performance.<sup>26</sup> However, the formation of bulk nanoporous Au-based alloys with a specific nanostructure, *e.g.*, core-shell, and flexibility to tune their activity, and selectivity is in its infancy. In particular, the achievement of scaled-up monolithic self-supported electrodes, which is of paramount importance for the practical implementation of nanoporous metals, still remains a challenge.

Herein, we synthesized monolithic self-supported nanoporous core-shell AuCu<sub>3</sub>@Au *via* the mild oxidative etching of the Au<sub>20</sub>Cu<sub>80</sub> alloy. The core-shell structure not only makes the Au nanolayers on the surface form Au-Au bonds, but also facilitates the electron transfer between the adjacent Cu atoms, thereby reducing the surface coordination number and providing abundant concave defects. The unsaturated coordination environment of the shell Au and curved interfaces generate a large number of highly active step sites for CO<sub>2</sub> conversion, decreasing the Gibbs free energy for the formation of \*COOH, and thus the onset potential. The as-prepared nanoporous AuCu<sub>3</sub>@Au could be directly utilized as a working electrode for the CO<sub>2</sub> RR, which is capable of reducing CO<sub>2</sub> to CO with an FE of up to 97.27% and partial current density of 5.3 mA cm<sup>-2</sup> at a low potential of -0.6 V vs. RHE. These values are much higher than that for nanoporous gold, implying that the core-shell nanoporous AuCu<sub>3</sub>@Au concurrently possesses the merits of high selectivity and low cost. Furthermore, it can maintain a high FE of CO in a broad potential window. Moreover, a 23 cm long and flexible electrode was easily made, which exhibited a high FE towards the CO<sub>2</sub> RR (Fig. S1 and S2†). The active current reached up to 37.2 mA (current density of 10.78 mA cm<sup>-2</sup>) at -0.7 V vs. RHE. Furthermore, the electrode exhibited no loss in activity after a reaction lasting 100 h, showing its promising practical application. Density functional theory (DFT) calculations revealed that the nanoshell Au in the porous AuCu<sub>3</sub>@Au induces a lower surface binding energy of intermediates, such as \*COOH and \*CO, by modifying the d-band centre of AuCu<sub>3</sub>, facilitating the formation of CO. This work highlights a promising strategy to design bulk monolithic electrode towards the practical applications of electrocatalysts, propelling the industrialization of the CO<sub>2</sub> RR.

## 2. Results and discussion

The phase and crystalline structure of AuCu<sub>3</sub>@Au was investigated *via* powder X-ray diffraction (XRD). As shown in Fig. 1a,

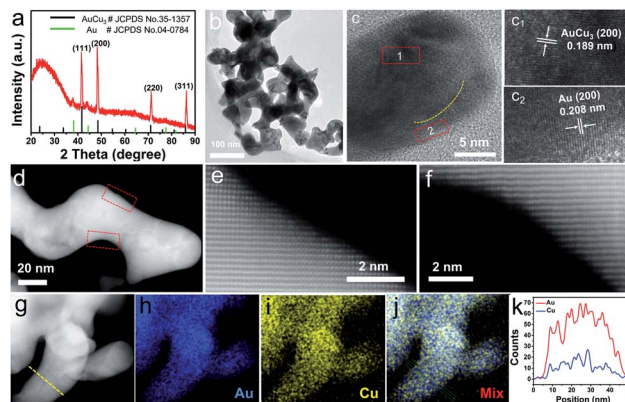


Fig. 1 Microstructures of the AuCu<sub>3</sub>@Au electrocatalyst. (a) XRD pattern of the as-prepared AuCu<sub>3</sub>@Au nanoporous alloy, (b and c) HRTEM images, (d) low-magnification HAADF image of the electrocatalyst, (e) atom-resolution image of the convex area of the marked in (d) HAADF, (f) atom-resolution image of HAADF concave area, and (g–j) STEM-EDS elemental mapping of AuCu<sub>3</sub>@Au nanoporous alloy. (k) Line profiles of Au and Cu recorded along the dashed line highlighted in (g).

the four characteristic peaks at 41.679°, 48.520°, 71.047°, and 85.891° can be assigned to the (111), (200), (220), and (311) planes of the face-centered cubic (FCC) AuCu<sub>3</sub>@Au, respectively. Compared with single Au, the peaks shifted to higher angles, indicating that Cu was incorporated into the Au lattice to form an alloy phase with concomitant lattice contraction.<sup>27</sup> In addition, it was noted that the small diffraction peaks coincided with fcc Au, implying the existence of Au nanolayers in AuCu<sub>3</sub>. The SEM and HRTEM images clearly reveal three-dimensional (3D) bicontinuous nanoporous structures with a ligament size of 40 nm (Fig. 1b and S3†). Furthermore, the HRTEM image (Fig. 1c) reveals that AuCu<sub>3</sub> is coated with a thin layer of Au on the surface with an average thickness of 1.7 nm. The lattice spacing of 0.208 nm corresponds to the (200) plane of Au, and the inner lattice spacing of 0.189 nm is the (200) plane for AuCu<sub>3</sub> (Fig. 1c<sub>1</sub> and c<sub>2</sub>, respectively). The low magnification TEM image (Fig. 1d) reveals that most of the ligaments possess positive, negative, and saddle-like curvatures, which is different from common nanoparticles with relatively well-defined shapes and only convex surface curvature at the corners.<sup>28,29</sup> The atomic resolution HAADF image and the corresponding fast Fourier transfer (FFT) pattern show abundant high-index facets with surface atomic steps on the edges (Fig. S4†). The presence of a high density of atomic steps and kinks on the surface of the concave and convex curvatures originates from the distinctive geometrical arrangement of the surface atoms of Au (Fig. 1e and f),<sup>26</sup> which are often chemically active sites. The EDX elemental mapping (Fig. 1g–j) illustrates that the Au and Cu atoms are distributed throughout the ligament. It can be seen from the integration diagram that the surface gold content is very rich. The linear scanning map (Fig. 1k) reveals that the gold signals on the margins are stronger than that in the middle region. While, the copper signal shows the reverse trend, proving the presence of a core-shell structure. The scan mode over the

surface element distribution (Fig. S5†) also demonstrates the surface is Au, which further shows the existence of Au ultrathin nanoshells.

XPS was performed to investigate the shell–core composition and chemical valence state. Fig. 2a and b present the high-resolution spectra of Au 4f and Cu 2p. For the AuCu<sub>3</sub>@Au surface, the Au 4f core levels can be split into two spin-orbit pairs at 83.5 and 87.2 eV, corresponding to metallic Au 4f<sub>7/2</sub> and 4f<sub>5/2</sub>, respectively. Similarly, the binding energies (BEs) of Cu 2p<sub>3/2</sub> and Cu 2p<sub>1/2</sub> are located at 932.18 and 951.70 eV, respectively. The positions of Au 4f<sub>7/2</sub> and 4f<sub>5/2</sub> in the nanoporous alloy slightly shift to a higher B.E. compared to that of the pure nanoporous Au. This is because the gold atoms interact with the copper atoms, and the electrons are redistributed to form an alloy with a different electron negativity.<sup>30</sup> Fig. 2c shows that the surface Au content is 64.29%, and the copper content is 35.71%. The copper on the interface is still in the state of Cu(0), while the small signals at 934.48 eV and 953.78 eV are attributed to CuO, which are caused by the inevitable oxidation during sample processing.<sup>31–33</sup> In addition, a significant negative shift for the band positions of Cu 2p<sub>3/2</sub> and Cu 2p<sub>1/2</sub> occurs relative to pure copper. This phenomenon illustrates that the interface copper hardly bonds with gold on the surface.<sup>34</sup> In the in-depth test, the ratio of Au/Cu changed significantly with the Au content of 39.2% and Cu content of 60.8%. The B.E.s of Au 4f<sub>7/2</sub> and 4f<sub>5/2</sub> shifted to a higher binding energy compared to that over the pure nanoporous Au (Fig. 2a and S6†). On the contrary, the B.E.s of Cu 2p<sub>3/2</sub> and Cu 2p<sub>1/2</sub> shifted to the opposite direction (Fig. 2b and S7†). It is reasonable that the electron transfer occurred from the Cu atom to Au atom, that is, the Cu atoms serve as the electron donor and more charges accumulated on Au. This decrease in B.E. reflects the downshift of the d-band center of the Cu atoms, resulting in the weak chemisorption of oxygen-containing species, *e.g.*, CO<sub>ads</sub> and OH<sub>ads</sub>, on the Au–Cu surface and contributes to the catalytic activity.<sup>13,35–37</sup>

To gain more insight into the correlation of the detailed surface structures with their electrochemical properties, we carried out XANES studies of the nanoporous electrocatalysts. Fig. 3a shows the normalized XANES spectra collected from the sample at the Au L<sub>3</sub> edge. Compared to the spectra of the reference foil, the Au edges over the XANES profile of AuCu<sub>3</sub>@Au have a similar edge shape to that of the Au foil reference, indicating its full Au(0) state.<sup>38</sup> In addition, the Au L<sub>3</sub>

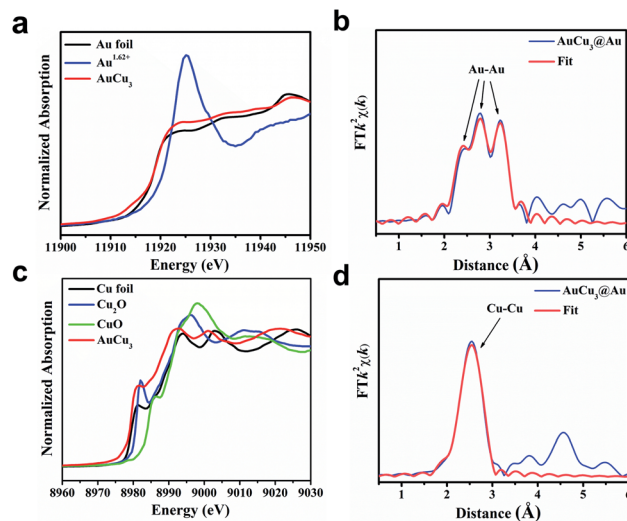


Fig. 3 X-ray absorption fine structure spectra of AuCu<sub>3</sub>@Au. (a) XANES profiles at the Au L<sub>3</sub>-edge. (b) EXAFS spectra at the Au L<sub>3</sub>-edge. (c) XANES profiles at the Cu K-edge. (d) EXAFS spectra at the Cu K-edge.

edge of XANES from the nanoporous AuCu<sub>3</sub>@Au shows a small increase in intensity compared to the Au foil in the region of 11 920–11 940 eV. This is where the “white line” absorption occurs, indicating an increase in electron density in the d-band of Au. The magnitude of the change in the white line is consistent with that in bulk AuCu alloy.<sup>39</sup> In addition, the edge position has a small shift to a higher photon energy compared with that of the Au foil. The phenomenon at the two edges is caused by the electron transfer from Cu to Au, which is consistent with the XPS analysis. The loss of electrons in the Cu d-band is compensated by a gain in the s–p bands.<sup>40</sup> According to Fig. 3c, copper is in the form of the metallic Cu<sup>0</sup> state. EXAFS with the data-fitting in *R* space was carried out to determine the short-range local coordination structure, including the distance (*R*) and coordination number (CN), around the gold and copper atoms. Based on the EXAFS fitting results (Fig. 3b, d, S8 and Table S1†), two local coordination structures around the Au and Cu centers matched perfectly. In total, three contributions from Au–Au (Au L<sub>3</sub>-edge), Cu–Cu (Cu K-edge) and Au–Cu/Cu–Au (Au L<sub>3</sub>-edge and Cu K-edge) can be identified. In particular, the strong peaks in the range of 1.5–3.5 Å can be assigned to the major Au–Au (CN: 7.6) and minor Au–Cu (CN: 0.6), as revealed by HRTEM and XPS. The surface gold led to a decrease in the average coordination number of 8.2 in total for AuCu<sub>3</sub>@Au compared to that of the Au foil (CN = 12). The thickness of the shell was estimated to be 1–2 nm,<sup>21</sup> which is consistent with the HRTEM observation. The unsaturated coordination environment of the ultrathin Au nanolayer, the curved surface with fruitful active sites, and intrinsic good conductivity enable the as-synthesized nanoporous AuCu<sub>3</sub>@Au to be used as an efficient electrocatalyst towards the CO<sub>2</sub> RR.

The as-obtained sample was directly applied as a monolithic electrode for the CO<sub>2</sub> RR. Fig. 4a presents the linear sweep voltammetry (LSV) curves in an N<sub>2</sub> and CO<sub>2</sub> atmosphere over the nanoporous AuCu<sub>3</sub>@Au electrode. The applied potential was in

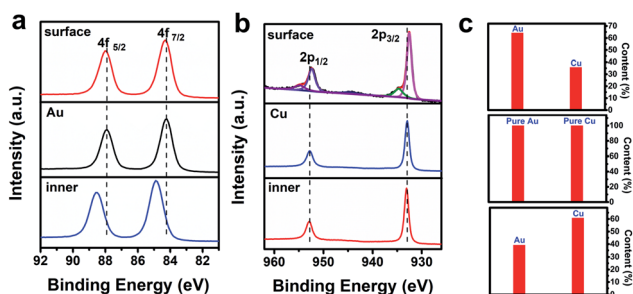


Fig. 2 High-resolution XPS spectra of surface nanoporous AuCu<sub>3</sub>@Au, pure Au, pure Cu and inner nanoporous AuCu<sub>3</sub>@Au. (a) Au 4f region, (b) Cu 2p region, and (c) Au and Cu content diagram.

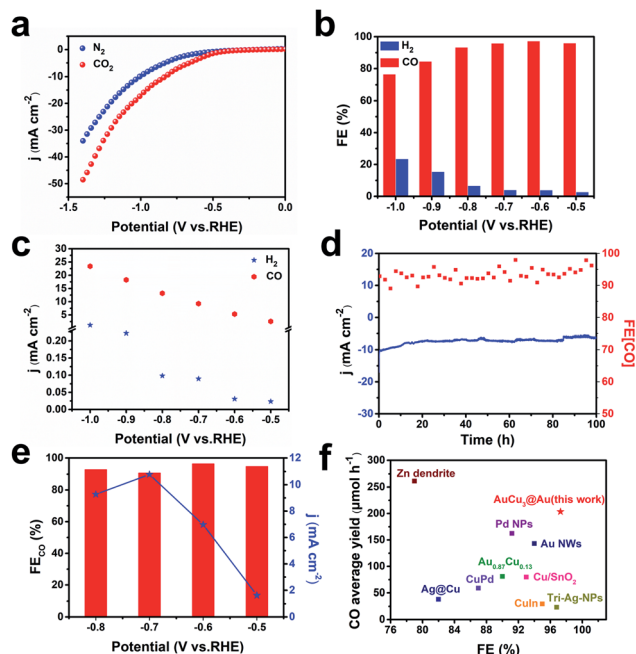


Fig. 4 Electrocatalytic CO<sub>2</sub> RR performance of AuCu<sub>3</sub>@Au. (a) LSV in N<sub>2</sub> and CO<sub>2</sub>-saturated 0.1 M KHCO<sub>3</sub> over AuCu<sub>3</sub>@Au, suggesting that a catalytic reaction occurs when CO<sub>2</sub> is present. (b) FE of H<sub>2</sub> and CO under different applied potentials. (c) Partial currents of CO and H<sub>2</sub> production at various potentials. (d) CO<sub>2</sub> RR stability test at the current density at  $-0.7$  V vs. RHE for 100 h continuous operation. (e) Determination of the FE of CO at a high current density. (f) Comparison with recent progress on CO production rates and faradaic efficiencies.

the range of  $0$ – $1.4$  V (vs. RHE) at a sweep rate of  $50$  mV s<sup>-1</sup>. The overall current density also contains the hydrogen evolution reaction (HER). A significant difference was observed in the LSV curves of AuCu<sub>3</sub>@Au between N<sub>2</sub>- and CO<sub>2</sub>-saturated electrolytes. The current densities (reaction activity) significantly increased in the CO<sub>2</sub>-saturated electrolyte, showing the significant contribution of the CO<sub>2</sub> RR. Thus the core-shell nanoporous AuCu<sub>3</sub>@Au exhibits high activity towards CO<sub>2</sub> conversion. Thereafter, stepped-potential tests were conducted in the potential range of  $-0.5$  to  $-1.0$  V (vs. RHE). As shown in Fig. 4b, CO and H<sub>2</sub> were the major products with the total FE approaching 100%. As the potential became more positive, the FE of CO increased while the HER was suppressed. The CO<sub>2</sub>-to-CO conversion was initiated from  $-0.5$  V vs. RHE, which rapidly increased to the conversion ratio of 96.03%, and reached an FE of 97.27% at  $-0.6$  V vs. RHE, which is 1.45 times of that over single nanoporous Au (Fig. S9–S13†). In contrast, the performance of single nanoporous Au was greatly affected by the applied potential. For example, when the potential increased to  $-1.1$  V vs. RHE, the FE of CO decreased to 47.2% with the dominant product of H<sub>2</sub>. However, for the nanoporous AuCu<sub>3</sub>@Au, it exhibited strong capacity to maintain a high FE of CO in a broad potential window. Moreover, the potential required at the highest FE was much lower than that of nanoporous Au ( $-0.6$  V vs.  $-0.8$  V). To ensure the FE, three tests were averaged at each potential, as shown in Fig. S14.† Fig. 4c shows a comparison of the partial current density for CO and H<sub>2</sub>

production. It can be seen that the partial current density for CO remarkably increased with an increase in voltage, indicating that the reaction rate of the CO<sub>2</sub> RR is accelerated at high potentials.<sup>41</sup> The partial current density for H<sub>2</sub> displayed a similar trend with approximately  $1.15$  mA cm<sup>-2</sup> at  $-1$  V vs. RHE (where, the partial current density of CO is  $23.39$  mA cm<sup>-2</sup>). Under the same overpotential, it is reported that about one third of the current density of H<sub>2</sub> is occupied over Au,<sup>42</sup> thus demonstrating the high activity of the as-synthesized AuCu<sub>3</sub>@Au.

To illustrate the improved electrocatalytic activity, we compared the electrochemically active surface area (ECSA) of nanoporous Au and nanoporous AuCu<sub>3</sub>@Au. Fig. S15a and c† present the obtained CV curves over nanoporous Au and nanoporous AuCu<sub>3</sub>@Au at different scan rates (from  $10$  to  $90$  mV s<sup>-1</sup> in  $20$  mV s<sup>-1</sup> increments), respectively, which were measured in a potential range without a faradaic process.<sup>43</sup> The corresponding capacitive current densities are plotted as a function of scan rate, as shown in Fig. S15b and d,† respectively. As a result, the specific capacitance of nanoporous Au ( $16.32$  mF cm<sup>-2</sup>) is about 20 times larger than that of the nanoporous AuCu<sub>3</sub>@Au ( $0.82$  mF cm<sup>-2</sup>). The ECSA of nanoporous Au was determined to be  $408.12$  cm<sup>2</sup>, which is about 20 times that of the nanoporous AuCu<sub>3</sub>@Au ( $20.57$  cm<sup>2</sup>). Then the change in the total current density of Au and AuCu<sub>3</sub>@Au over time was investigated at different potentials. As shown in Fig. S16,† the current fluctuated dramatically over nanoporous Au at a high overpotential (more negative potential) due to the vigorous HER, which blocks the active sites on the electrodes. In contrast, the total current density over the nanoporous AuCu<sub>3</sub>@Au remained stable even at high overpotentials (Fig. S17†). Therefore, although the nanoporous Au has a larger ECSA, the current density of the nanoporous AuCu<sub>3</sub>@Au is more than 40 times that of the nanoporous Au at the same potential. For example, the total current density at  $-1.0$  V vs. RHE over the nanoporous AuCu<sub>3</sub>@Au ( $0.23$  mA cm<sub>ECSA</sub><sup>-2</sup>) is much higher than that over Au ( $0.0048$  mA cm<sub>ECSA</sub><sup>-2</sup>), further proving the high performance over the nanoporous AuCu<sub>3</sub>@Au. Additionally, the surface roughness of the nanoporous Au and AuCu<sub>3</sub>@Au was also analyzed *via* atomic force microscopy (AFM, Fig. S18†), revealing that the surface roughness of the nanoporous Au is higher than that of the nanoporous AuCu<sub>3</sub>@Au. This is consistent with the ECSA analyses. Thus, the synergistic effect of Au and Cu in the nanoporous AuCu<sub>3</sub>@Au is more beneficial towards the CO<sub>2</sub> RR in comparison with nanoporous Au. After the reaction was complete, as revealed in Fig. S19 and S20,† the structure of the used AuCu<sub>3</sub>@Au electrode has no obvious change. Even after electrolysis for 100 h at a potential of  $-0.7$  V, the total current density over the catalyst was still maintained at  $\sim 10$  mA cm<sup>-2</sup> (Fig. 4d), suggesting a stable reaction. The SEM images (Fig. S21†) of the collected nanoporous AuCu<sub>3</sub>@Au sample show that it still retained its pristine porous structure, implying its good stability. The CVs of Au and AuCu<sub>3</sub> before and after electrolysis also show the nanoporous structures were well maintained (Fig. S22†).

Considering practical applications, we further prepared a bulk nanoporous AuCu<sub>3</sub>@Au electrode with a length of  $23$  cm and width of  $0.15$  cm (Fig. S2†). The active current reached up to

37.2 mA with a current density of 10.78 mA cm<sup>-2</sup> at -0.7 V vs. RHE (Fig. 4e and S23†) while promising a high FE of CO, pushing industrialization in comparison with powder samples. Furthermore, the CO production rate over the nanoporous AuCu<sub>3</sub>@Au exceeds that of most of the reported similar electrocatalysts (Fig. 4f and Table S2†).

The reaction mechanism of the CO<sub>2</sub> RR on the surface of the Au {311} and AuCu<sub>3</sub>@Au {311} catalysts was calculated to give insight into the process. As shown in Fig. 5a, the results show that the free energy change for the formation of the \*COOH intermediate on the AuCu<sub>3</sub>@Au {311} catalyst is significantly lower than that on the Au {311} catalyst. This is mainly because in the AuCu<sub>3</sub>@Au {311} catalyst, both metallic Au and Cu can simultaneously interact with the \*COOH intermediate, while only one Au atom interacts with the \*COOH intermediate in Au {311} (Fig. 5c and d), respectively. This double-dentate adsorption in AuCu<sub>3</sub>@Au effectively improves the stability of the \*COOH intermediate. The density of states analysis also indicates that the introduction of Cu can cause the d-band-centre of AuCu<sub>3</sub>@Au to move toward the Fermi level, making it directly bond with \*COOH (Fig. 5b). Therefore, the adsorption of \*COOH on the surface of AuCu<sub>3</sub>@Au {311} is strengthened,<sup>44</sup> which stabilizes the \*COOH intermediate, facilitating the formation of CO.<sup>17</sup>

### 3. Experimental

#### 3.1 Materials synthesis

The Au<sub>20</sub>Cu<sub>80</sub> alloy was prepared *via* the arc melting technique (WK type, Physcience Opto-electronics Co., Ltd., Beijing). In a typical procedure, pure metals of Cu (99.999 wt%), and Au (99.999 wt%) were melted 3 times on a water-cooled copper hearth under a Ti-gettered argon atmosphere. The pre-alloyed ingot was remelted in a quartz tube by high-frequency induction heating on a melt spinning equipment (WK-IIB type, Physcience Opto-electronics Co., Ltd., Beijing). Then the melt was injected onto a copper roller with a diameter of 25 cm, which was rotated at a speed of ~3000 rpm in a controlled argon

atmosphere. The as-spun alloy ribbons were ~25 μm in thickness, 1.5 mm in width and 20 cm in length, respectively.

For the preparation of the monolithic nanoporous core-shell AuCu<sub>3</sub>@Au electrode, 40 mg of Au<sub>20</sub>Cu<sub>80</sub> was immersed in 5 mM of FeCl<sub>3</sub> aqueous solution at room temperature under stirring for 30 min. Then the obtained sample was rinsed with deionized water several times, and dried in a vacuum oven at 60 °C for 12 h. For comparison, pure nanoporous Au was also prepared when the FeCl<sub>3</sub> concentration was increased to 0.5 M and the other conditions were kept constant.

#### 3.2 Material characterization

Powder X-ray diffraction (XRD) data were collected on a Rigaku Corporation UltimaIV X-ray diffractometer using Cu K $\alpha$  irradiation ( $\lambda = 1.5406 \text{ \AA}$ ). The morphology and microstructures were characterized on an FEI Verious 460L field-emission scanning electron microscope (SEM; ZEISS MERLIN Compact, Germany), transmission electron microscope (TEM, TecnaiG2 Spirit TWIN, FEI), high-resolution transmission electron microscope (HRTEM) with FEG (Talos F200 X), and high-angle annular dark field scanning transmission electron microscope (Titan Themis Cubed G2 60-300) instruments equipped with an Oxford SDD X-Max energy dispersive X-ray spectrometer (EDS). The surface composition was analyzed with a THERMO SCIENTIFIC ESCA-LAB250xi X-ray photoelectron spectrometer (XPS), using monochromatized Al K $\alpha$  X-rays as the excitation source, and C 1s (284.80 eV) as the reference line. The surface roughness was measured with an atomic force microscope (AFM, Dimension icon, Bruker, Germany).

The X-ray absorption fine structure (XAFS) spectra at the Au L<sub>3</sub> ( $E_0 = 11\,919.0 \text{ eV}$ ) and Cu K ( $E_0 = 8979.0 \text{ eV}$ ) edge were measured at the BL14W1 beamline of the Shanghai Synchrotron Radiation Facility (SSRF) operated at 3.5 GeV under “top-up” mode with a constant current of 260 or 200 mA. The XAFS data were recorded under transmission mode with two Oxford ion chambers or fluorescence mode with a Lytle ion chamber. The energy was calibrated according to the absorption edge of pure Au or Cu foil. Athena and Artemis codes were used to extract the data and fit the profiles. For the X-ray absorption near edge structure (XANES), the experimental absorption coefficients as a function of energy,  $\mu(E)$ , were processed by background subtraction and normalization procedures, and reported as “normalized absorption” with  $E_0 = 11\,919.0$  or  $8979.0 \text{ eV}$  for the measured sample and standard Au/Cu foil. For the extended X-ray absorption fine structure (EXAFS), the Fourier transformed (FT) data in  $R$  space was analyzed by applying the first-shell approximate model for the Au-Cu or Cu-Au contribution, and metallic Au or Cu model for the Au-Au or Cu-Cu contribution. The passive electron factor,  $S_0^2$ , was determined by fitting the experimental data on Au or Cu foil and fixing the coordination number (CN) of Au-Au or Cu-Cu to be 12, and then fixed for further analysis of the tested samples. The parameters describing the electronic properties (*e.g.*, correction to the photoelectron energy origin,  $E_0$ ) and local structure environment including CN, bond distance ( $R$ ) and Debye-Waller factor around the absorbing atoms were allowed to vary

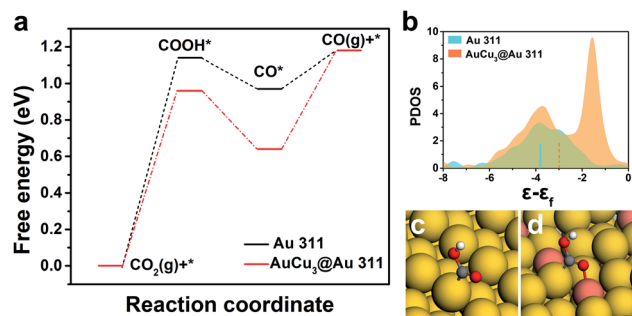


Fig. 5 Theoretical investigations of the CO<sub>2</sub> RR on Au{311} and AuCu<sub>3</sub>@Au {311}. (a) Gibbs free changes of the intermediates of the CO<sub>2</sub> RR on Au{311} and AuCu<sub>3</sub>@Au {311}, (b) partial density of states of Au and Cu at the adsorption sites of \*COOH. The dotted and dashed lines are for the d band centre of “Au 311” and “AuCu<sub>3</sub>@Au 311”, respectively. (c) Adsorption structure of \*COOH on Au{311}, and (d) adsorption structure of \*COOH on AuCu<sub>3</sub>@Au {311}.

during the fit process. The fitted ranges for the  $k$  and  $R$  spaces were selected to be  $k = 3\text{--}12 \text{ \AA}^{-1}$  (Au) or  $3\text{--}11.5 \text{ \AA}^{-1}$  (Cu) with  $R = 1.5\text{--}3.5 \text{ \AA}$  (Au) or  $1.0\text{--}3.0 \text{ \AA}$  (Cu) ( $k^2$  weighted).

### 3.3 Electrochemical measurements

All electrochemical tests were performed on a CHI 760E electrochemical workstation at room temperature. A three-electrode system was used with the self-supported monolithic nanoporous sample as the working electrode and Pt as the counter electrode. All potentials were measured against an Ag/AgCl reference electrode (3.0 M KCl), and converted to the RHE reference scale using the equation  $E$  (vs. RHE) =  $E$  (vs. Ag/AgCl) + 0.1989 V + 0.0591 V  $\times$  pH. The CO<sub>2</sub> RR was used to probe the electrocatalytic performance over the nanoporous electrode. The tests were performed in a two-compartment electrochemical cell with a piece of anion exchange membrane (Nafion®117) as the separator. The electrolyte was 0.1 M KHCO<sub>3</sub> saturated with CO<sub>2</sub> at a pH of 6.8. Each compartment contained 40.0 mL of electrolyte. Before the reaction was initiated, the electrolyte in the cathodic compartment was bubbled with CO<sub>2</sub> gas for at least 30 min. Magnetic stirring was applied at a rate of 500 rpm throughout the whole test.

### 3.4 CO<sub>2</sub> RR evaluation

CO<sub>2</sub> gas was bubbled into the cathodic compartment at an average rate of 10 sccm (at room temperature and ambient pressure), which was vented directly into the gas sampling loop of a gas chromatograph (GC9790II, Zhejiang Fuli Analyzing Instruments Co. Ltd.). GC was initiated every 25 min, and nitrogen (99.999%) was used as the carrier gas. The separated gas mixtures were passed through a thermal conductivity detector (TCD), where the concentration of hydrogen was analyzed, and the concentration of CO was analyzed by a flame ionization detector (FID) with a methanizer.

### 3.5 Computation details

DFT calculations were performed using the DMol<sub>3</sub> code.<sup>45,46</sup> The generalized gradient approximation (GGA) was treated by the Perdew, Burke and Ernzerhof (PBE) method.<sup>47</sup> Double numerical plus polarization (DNP) was used as the basis set. The inner electrons of the Au atoms were treated by a DFT semi-core pseudopotential. The convergence criteria were set to be  $1 \times 10^{-5}$  Ha,  $0.001 \text{ Ha \AA}^{-1}$ , and  $0.005 \text{ \AA}$  for energy, force, and displacement convergence, respectively. A self-consistent field (SCF) density convergence with a threshold value of  $1 \times 10^{-5}$  Ha was specified. The real-space global orbital cut-off radius was set as  $4.5 \text{ \AA}$ . The Au{311} and AuCu<sub>3</sub>@Au {311} catalysts were modelled using  $(8.85 \text{ \AA} \times 10.22 \text{ \AA} \times 9.81 \text{ \AA})$  and  $(14.98 \text{ \AA} \times 11.53 \text{ \AA} \times 8.61 \text{ \AA})$  supercells. The vacuum layer was set to be  $30 \text{ \AA}$ .

## 4. Conclusions

In summary, we developed a mild oxidative etching method to synthesize core-shell three-dimensional nanoporous AuCu<sub>3</sub>@Au at room temperature. The unsaturated coordination environment and curved interfaces provide abundant active sites,

enabling the as-obtained nanoporous AuCu<sub>3</sub>@Au to be applied as an efficient electrocatalyst towards the CO<sub>2</sub> RR. The as-obtained monolithic nanoporous Au@AuCu<sub>3</sub> was directly utilized as an electrode to convert CO<sub>2</sub> to CO in a broad potential window, over which the CO FE reached 97.27% at  $-0.6 \text{ V}$  with the current density of  $5.3 \text{ mA cm}^{-2}$ . This value is 1.45 times that in nanoporous Au. Moreover, the nanoporous AuCu<sub>3</sub>@Au exhibited long-term stability without loss in its performance after a 100 h duration test. The double-dentate adsorption in AuCu<sub>3</sub>@Au effectively improves the stability of the \*COOH intermediate. The introduction of Cu can cause the d-band-centre of the atom to directly bond with \*COOH, enhancing the adsorption of \*COOH on the surface of AuCu<sub>3</sub>@Au {311}, and facilitating the formation of CO. Importantly, a bulk nanoporous AuCu<sub>3</sub>@Au electrode with a length of 23 cm was obtained easily, with the current reaching 37.2 mA with a current density of  $10.78 \text{ mA cm}^{-2}$  at  $-0.7 \text{ V}$  vs. RHE, propelling the industrialization of the CO<sub>2</sub> RR. This work can be extended to the synthesis of other types of efficient electrocatalysts by carefully varying the composition, and microstructures of the nanoporous alloys.

## Conflicts of interest

There are no conflicts to declare.

## Acknowledgements

The authors gratefully acknowledge the financial support by the National Natural Science Foundation of China (21771137, 21773288 and 21971190), the Key Project of Natural Science Foundation of Tianjin (Contract No. 18JCZDJC97200), and the Training Project of Innovation Team of Colleges and Universities in Tianjin (TD13-5020).

## Notes and references

- G. A. Olah, G. K. Prakash and A. Goeppert, *J. Am. Chem. Soc.*, 2011, **133**, 12881–12898.
- J. H. Montoya, L. C. Seitz, P. Chakhranont, A. Vojvodic, T. F. Jaramillo and J. K. Norskov, *Nat. Mater.*, 2016, **16**, 70–81.
- B. A. Rosen, A. Salehi-Khojin, M. R. Thorson, W. Zhu, D. T. Whipple, P. J. Kenis and R. I. Masel, *Science*, 2011, **334**, 643–644.
- M. Liu, Y. Pang, B. Zhang, P. De Luna, O. Voznyy, J. Xu, X. Zheng, C. T. Dinh, F. Fan, C. Cao, F. P. de Arquer, T. S. Safaei, A. Mepham, A. Klinkova, E. Kumacheva, T. Filleter, D. Sinton, S. O. Kelley and E. H. Sargent, *Nature*, 2016, **537**, 382–386.
- Y. Hori, A. Murata, K. Kikuchi and S. Suzuki, *J. Chem. Soc., Chem. Commun.*, 1987, **10**, 728–729.
- A. S. Hall, Y. Yoon, A. Wuttig and Y. Surendranath, *J. Am. Chem. Soc.*, 2015, **137**, 14834–14837.
- H. Mistry, R. Reske, Z. Zeng, Z. J. Zhao, J. Greeley, P. Strasser and B. R. Cuenya, *J. Am. Chem. Soc.*, 2014, **136**, 16473–16476.
- Y. Chen, C. W. Li and M. W. Kanan, *J. Am. Chem. Soc.*, 2012, **134**, 19969–19972.

- 9 W. Zhu, R. Michalsky, O. Metin, H. Lv, S. Guo, C. J. Wright, X. Sun, A. A. Peterson and S. Sun, *J. Am. Chem. Soc.*, 2013, **135**, 16833–16836.
- 10 W. Zhu, Y. J. Zhang, H. Zhang, H. Lv, Q. Li, R. Michalsky, A. A. Peterson and S. Sun, *J. Am. Chem. Soc.*, 2014, **136**, 16132–16135.
- 11 T. Saberi Safaei, A. Mepham, X. Zheng, Y. Pang, C. T. Dinh, M. Liu, D. Sinton, S. O. Kelley and E. H. Sargent, *Nano Lett.*, 2016, **16**, 7224–7228.
- 12 S. Back, M. S. Yeom and Y. Jung, *ACS Catal.*, 2015, **5**, 5089–5096.
- 13 D. Kim, J. Resasco, Y. Yu, A. M. Asiri and P. Yang, *Nat. Commun.*, 2014, **5**, 4948.
- 14 S. Ma, M. Sadakiyo, M. Heima, R. Luo, R. T. Haasch, J. I. Gold, M. Yamauchi and P. J. A. Kenis, *J. Am. Chem. Soc.*, 2016, **139**, 47–50.
- 15 K. Sun, L. Wu, W. Qin, J. Zhou, Y. Hu, Z. Jiang, B. Shen and Z. Wang, *J. Mater. Chem. A*, 2016, **4**, 12616–12623.
- 16 J. Li, S. Z. Jilani, H. Lin, X. Liu, K. Wei, Y. Jia, P. Zhang, M. Chi, Y. J. Tong, Z. Xi and S. Sun, *Angew. Chem., Int. Ed.*, 2019, **5**, 11527–11533.
- 17 K. Liu, M. Ma, L. Wu, M. Valenti, D. Cardenas-Morcoso, J. P. Hofmann, J. Bisquert, S. Gimenez and W. A. Smith, *ACS Appl. Mater. Interfaces*, 2019, **11**, 16546–16555.
- 18 Z. Weng, X. Zhang, Y. Wu, S. Huo, J. Jiang, W. Liu, G. He, Y. Liang and H. Wang, *Angew. Chem., Int. Ed.*, 2017, **56**, 13135–13139.
- 19 Y. Ding, A. Mathur, M. Chen and J. Erlebacher, *Angew. Chem., Int. Ed.*, 2005, **117**, 4070–4074.
- 20 A. L. Strickler, M. A. Escudero-Escribano and T. F. Jaramillo, *Nano Lett.*, 2017, **17**, 6040–6046.
- 21 C. Wang, M. Chi, D. Li, D. Strmcnik, D. van der Vliet, G. Wang, V. Komanicky, K. C. Chang, A. P. Paulikas, D. Tripkovic, J. Pearson, K. L. More, N. M. Markovic and V. R. Stamenkovic, *J. Am. Chem. Soc.*, 2011, **133**, 14396–14403.
- 22 K. Sun, T. Cheng, L. Wu, Y. Hu, J. Zhou, A. Maclennan, Z. Jiang, Y. Gao, W. A. Goddard III and Z. Wang, *J. Am. Chem. Soc.*, 2017, **139**, 15608–15611.
- 23 M. F. Alqahtani, K. P. Katuri, S. Bajracharya, Y. Yu, Z. Lai and P. E. Saikaly, *Adv. Funct. Mater.*, 2018, **28**, 1804860.
- 24 S. Zhao, R. Jin and R. Jin, *ACS Energy Lett.*, 2018, **3**, 452–462.
- 25 Q. Lu, J. Rosen, Y. Zhou, G. S. Hutchings, Y. C. Kimmel, J. G. Chen and F. Jiao, *Nat. Commun.*, 2014, **5**, 3242.
- 26 W. Zhang, J. He, S. Liu, W. Niu, P. Liu, Y. Zhao, F. Pang, W. Xi, M. Chen, W. Zhang, S. S. Pang and Y. Ding, *Nanoscale Adv.*, 2018, **10**, 8372–8376.
- 27 Q. Wang, S. Chen, F. Shi, K. Chen, Y. Nie, Y. Wang, R. Wu, J. Li, Y. Zhang, W. Ding, Y. Li, L. Li and Z. Wei, *Adv. Mater.*, 2016, **28**, 10673–10678.
- 28 T. Fujita, P. Guan, K. McKenna, X. Lang, A. Hirata, L. Zhang, T. Tokunaga, S. Arai, Y. Yamamoto, N. Tanaka, Y. Ishikawa, N. Asao, Y. Yamamoto, J. Erlebacher and M. Chen, *Nat. Mater.*, 2012, **11**, 775–780.
- 29 P. Liu, P. Guan, A. Hirata, L. Zhang, L. Chen, Y. Wen, Y. Ding, T. Fujita, J. Erlebacher and M. Chen, *Adv. Mater.*, 2016, **28**, 1753–1759.
- 30 H. Mistry, R. Reske, P. Strasser and B. Roldan Cuenya, *Catal. Today*, 2017, **288**, 30–36.
- 31 J. Wen, K. Wu, D. Yang, J. Tian, Z. Huang, A. S. Filatov, A. Lei and X.-M. Lin, *ACS Appl. Mater. Interfaces*, 2018, **10**, 25930–25935.
- 32 W. Luo, W. Xie, R. Mutschler, E. Oveisi, G. L. De Gregorio, R. Buonsanti and A. Züttel, *ACS Catal.*, 2018, **8**, 6571–6581.
- 33 Y. Lum and J. W. Ager, *Angew. Chem., Int. Ed.*, 2018, **57**, 551–554.
- 34 D. Ren, Y. Deng, A. D. Handoko, C. S. Chen, S. Malkhandi and B. S. Yeo, *ACS Catal.*, 2015, **5**, 2814–2821.
- 35 T. Bligaard and J. K. Nørskov, *Electrochim. Acta*, 2007, **52**, 5512–5516.
- 36 H. Wang, S. Yin, Y. Xu, X. Li, A. A. Alshehri, Y. Yamauchi, H. Xue, Y. V. Kaneti and L. Wang, *J. Mater. Chem. A*, 2018, **6**, 8662–8668.
- 37 C. Du, M. Chen, W. Wang, Q. Tan, K. Xiong and G. Yin, *J. Power Sources*, 2013, **240**, 630–635.
- 38 A. I. Frenkel, C. W. Hills and R. G. Nuzzo, *J. Phys. Chem. B*, 2001, **105**, 12689–12703.
- 39 M. Kuhn and T. K. Sham, *Phys. Rev. B: Condens. Matter Mater. Phys.*, 1994, **49**, 1647–1661.
- 40 J. C. Bauer, D. Mullins, M. Li, Z. Wu, E. A. Payzant, S. H. Overbury and S. Dai, *Phys. Chem. Chem. Phys.*, 2011, **13**, 2571–2581.
- 41 Z. Yin, D. Gao, S. Yao, B. Zhao, F. Cai, L. Lin, P. Tang, P. Zhai, G. Wang, D. Ma and X. Bao, *Nano Energy*, 2016, **27**, 35–43.
- 42 A. M. Ismail, E. Csapó and C. Janáky, *Electrochim. Acta*, 2019, **313**, 171–178.
- 43 B.-B. Chen, D.-K. Ma, Q.-P. Ke, W. Chen and S.-M. Huang, *Phys. Chem. Chem. Phys.*, 2016, **18**, 6713.
- 44 J. K. Nørskov, J. Rossmeisl, A. Logadottir, L. Lindqvist, J. R. Kitchin, T. Bligaard and H. Jónsson, *J. Phys. Chem. B*, 2004, **108**, 17886–17892.
- 45 B. Delley, *J. Chem. Phys.*, 2000, **113**, 7756–7764.
- 46 J. P. Perdew, K. Burke and M. Ernzerhof, Generalized Gradient Approximation Made Simple, *Phys. Rev. Lett.*, 1996, **77**, 3865–3868.
- 47 S. Grimme, J. Antony, S. Ehrlich and H. Krieg, *J. Chem. Phys.*, 2010, **132**, 154104.